REGRESSION ANALYSIS OF ERRORS OF SAR-BASED DEMS AND CONTROLLING FACTORS

Y.Y. Wu [1] *, H. Ren [2]

[1] Center for Space and Remote Sensing, National Central University, Taiwan – amily115308@gmail.com
[2] Center for Space and Remote Sensing, National Central University, Taiwan – hren@csrsr.ncu.edu.tw

KEY WORDS: InSAR, digital elevation model, water vapor variation, surface deformation, linear regression analysis.

ABSTRACT:

Interferometric Synthetic Aperture Radar (InSAR) has been well developed for several decades and is known for its powerful capability of retrieving three-dimensional ground information from SAR imagery. One of the most important application of InSAR technique is topographic mapping. The technique is limited when confronting certain poor conditions which lead to low coherence. In this research, we aim at investigating the relationship between SAR-based digital elevation models (DEMs) and related factors that contribute to the error budget by conducting a linear regression analysis. The surface deformation in line of sight (LOS) direction and the amount of integral refractivity change over two acquisition events are considered as two related factors. Eight pairs of Sentinel-1 images were selected to conduct InSAR processing over Chaiyi City of Taiwan, and SNAP software was used to generate SAR-based DEMs. The coherence mask was applied during the InSAR workflow in order to alleviate unwrapping error. The result has shown that the coherence thresholds help to improve the accuracy by up to 52.61%. Since some large errors were observed from the resulting InSAR-DEMs, these points were removed based on standard error. In regression analysis, there were 15 set of data, categorized by different coherence threshold and data removal standard, to test the model. As the result has shown, when the coherence threshold is 0.3 and the points were filtered with half standard error, the R^2 can achieve 0.85. However, the rest of the dataset did not produce desirable results. In our discussion, we have provided several reasons which might have contributed to this outcome.

1. INTRODUCTION

InSAR has been extensively used for decades to extract 3D information of a surface. One of the most important application of InSAR techniques is topographic mapping, which is essential for various purposes such as three-dimensional visualization, terrain analysis, disaster analysis and navigation. Despite many ways to generate a DEM, InSAR techniques allow users to obtain a high-resolution topographic map with areal coverage and at low cost in near-real-time, which makes it more attractive and feasible than other approaches. However, due to the unavoidable and inherent limitations of the SAR implementation, there are different challenges to be tackled depending on the purpose of the investigation. A few common issues that have been discussed are geometric decorrelation, temporal decorrelation, and atmospheric disturbance (Hanssen, 2001; Usai, 1997; Zebker and Villasenor, 1992). These obstacles could seriously deteriorate the quality of the final DEM products, depending on the selection of InSAR image pairs and the environmental conditions of the area of interest.

In previous research, some authors have discussed possible factors contributing to height error budget for topography mapping. The first investigation was done by Zebker and Goldstein (1986). They derived a topography map of San Francisco Bay Area using an airborne SAR system, and successfully obtained a 2-10 m Root Mean Square (RMS) error with assumptions about error sources of their experiment, such as errors from approximation, roll error, and inaccurate monitoring of aircraft attitude.

Later on, Li and Goldstein (1990) presented a model of errors regarding InSAR topography measurements. The errors that were discussed were all associated with the phase measurements, including signal-to-noise ratios (SNR), number of looks, pixel mis-registration and baseline decorrelation. Other research that assess the height error budget has been presented by Rodriguez and Martin (1992) who provided a more extended view towards the topic and separate the errors into two types, intrinsic height error and location induced errors.

However, most research until then has been focusing mainly on errors induced by the sensor, satellite positioning or processing accuracy. It was not until the work by Hanssen (2001) that a more comprehensive view of error analysis and data interpretation was provided. The book covers various types of errors in addition to the aforementioned ones, including atmospheric propagation and scattering characteristics.

Based on that work, we have derived a formal description that attempts to explain the relationship between SAR-measured elevation height and controlling factors. In this research, we want to additionally uncover the error contributed from surface deformation due to the frequency of earthquakes in Taiwan, together with the discussion of the influence from tropospheric delay.

To conclude, we aim at investigating the relationship between SAR-based DEMs and related factors which contribute to the error budget by conducting a linear regression analysis. The surface deformation in LOS direction and the amount of integral refractivity changes in the air column over two acquisition events are considered as two related factors in this paper.

Eight pairs of Sentinel-1 images were selected from the Copernicus Open Access Hub and processed with SNAP software (SNAP, 2020). Time series GPS data of Taiwan were collected from GPS LAB (Chen, 2019), a Taiwanese GPS network service. The three-dimensional vectors were extracted from time series GPS data to obtain the displacement in LOS

* Corresponding author

direction. Vertical integral refractivity data were acquired from the Weather Research and Forecasting model (WRF v3.8.1, Skamarock et al., 2008) developed based on work published by Liu et al. (2016).

2. STUDY SITE

The test site is located in Chiayi City and has an approximate area of 72 km^2 , of Taiwan (Figure 1). The test site is chosen due to two reasons: (1) the coherence value of urban area is relatively higher than other land cover types, which can reduce the impact of unwrapping errors; (2) Chiayi is located in Southern Taiwan with apparent wet and dry seasons, which could provide a more dispersed atmospheric conditions in favor of this research.

The areas are characterized by urban and industrial zones. In addition, there are several river systems discharging water from the mountain ranges into the Taiwan Straight in the West. The overall altitude ranges between 10 to 100 meters.

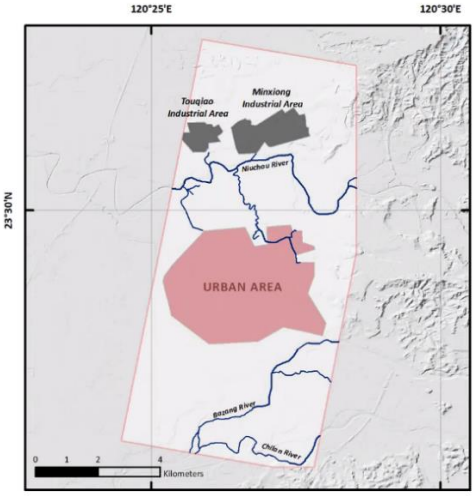

Figure 1. Test Site: Chiayi City of Taiwan.

3. METHODOLOGY

3.1 Problem Analysis

SAR is an active microwave imaging system which allows to records surface information in the form of amplitude and phase. Phase is measured as the distance between the sensor and the targets. From the variation of phase between two acquisition times, we can exploit either ground elevation or surface deformation.

The interferometric phase φ_p can be formed with Flat-Earth phase component ($\Delta\varphi_{flat}$), topographic phase component ($\Delta\varphi_{topo}$), deformation phase component ($\Delta\varphi_{defo}$), atmospheric phase component ($\Delta\varphi_{atmo}$), noise phase component ($\Delta\varphi_{noise}$), and the phase integer cycle ($2\pi k$). (Equation 1) (Hanssen, 2001; Hu et al., 2014)

$$\varphi_p = \Delta\varphi_{flat} + \Delta\varphi_{topo} + \Delta\varphi_{defo} + \Delta\varphi_{atmo} + \Delta\varphi_{noise} + 2\pi k \quad (1)$$

Since the orbit parameters can be used to remove the flat earth phase, and the noise can be reduced through Goldstein filtering, the interferometric phase change ($\Delta\varphi_p$) can be confined to equation (2). And then substitute each term with its estimated formula to derive equation (3).

$$\Delta\varphi_p = \Delta\varphi_{topo} + \Delta\varphi_{defo} + \Delta\varphi_{atmo} \quad (2)$$

$$\Delta\varphi_p = \frac{-4\pi}{\lambda}\left(D - \frac{B_\perp}{R\sin\theta}H + \frac{10^{-6}}{\cos\theta}\int_{h_1}^{h_{top}}\left(N_{hydr} + N_{wet}\right)dh\right) \quad (3)$$

where $\Delta\varphi_p$ = the interferometric phase change
λ = image coordinates
D = surface displacement in line of sight (LOS) direction
$B_\perp$ = perpendicular baseline
R = the signal path length (slant range)
θ = incidence angle
H = the measured height (ellipsoidal heights)
h_1 = the ground elevation
h_{top} = the top of the troposphere (tropopause)
N_{hydr} = hydrostatic component of the refractivity, N
N_{wet} = wet component of the refractivity, N

From equation (3), we can move the measured height to the left-hand side, and the remaining terms are moved and arranged at the right-hand side of the equation, so we can find equation (4), illustrating the relationship between the measured topography height and the total phase variation.

$$H = \frac{R\sin\theta}{B_\perp}\left(\frac{\lambda}{4\pi}\Delta\varphi_p + D + \frac{10^{-6}}{\cos\theta}\int_{h_1}^{h_{top}}\left(N_{hydr} + N_{wet}\right)dh\right) \quad (4)$$

Theoretically, if there is no surface deformation and atmospheric condition change during two acquisition time, then the measured height will simply be the transformation from the total phase variation to elevation. However, the reality is that the existence of surface deformation and atmospheric condition change are always there, influencing the total phase variation and thus producing errors to the measured elevation height. Therefore, H is composed of true elevation height (H_{real}) and the error produced by surface deformation and atmospheric condition change. Equation (4) can accordingly be rewritten as equation (5).

$$H_{real} + \varepsilon = \frac{R\sin\theta}{B_\perp}\left(\frac{\lambda}{4\pi}\Delta\varphi_p + D + \frac{10^{-6}}{\cos\theta}\int_{h_1}^{h_{top}}\left(N_{hydr} + N_{wet}\right)dh\right) \quad (5)$$

From equation (5), we can observe a linear relationship between error and the influencing factors, since the conversion of $\Delta\varphi_p$ on the right-hand side of the equation is basically the same as the real elevation height (H_{real}). Ultimately, we aim at finding the relationship in reality by exploiting Sentinel-1 imagery, surface deformation data and the atmospheric component.

3.2 Surface Deformation

Time series GPS data were downloaded from GPS LAB (Chen, 2019). The three-dimensional vectors were extracted from time series GPS data to convert vertical displacements to LOS direction using equation (6) (Hanssen, 2001).

$$d_r = d_u\cos(\theta) - \sin(\theta)\left[d_n\cos\left(\alpha_h - \frac{3\pi}{2}\right) + d_e\sin\left(\alpha_h - \frac{3\pi}{2}\right)\right] \quad (6)$$

where $d_n,\ d_e,\ d_u$ = the displacement vector in North, East, and Up direction, respectively
α_h = heading (azimuth) angle
d_r = the displacement in LOS direction

3.3 Tropospheric Delay

According to Bekaert et al. (2015), a phase delay through the atmosphere can be characterized by the refractivity, N (Wright et al., 2001), which can be derived from formula (7) (Smith and Weintraub, 1953; Thayer, 1974).

$$N = \left(k_1 \frac{P}{T}\right)_{hydr} + \left(k_2' \frac{e}{T} + k_3 \frac{e}{T^2}\right)_{wet} \quad (7)$$

where P = total atmospheric pressure
T = temperature
e = the partial pressure of water vapor

Applying formula (7), we can obtain the refractivity at a certain atmospheric layer. To acquire the total refractivity of the air column, the value needs to be integrated from ground elevation (h_1) to tropopause (h_{top}). Therefore, we applied the definition of World Meteorological Organization (Organisation météorologique, 1992) to define the height of tropopause and integrate the tropospheric delay in air column.

3.4 Coherence Mask

Phase unwrapping (PU) is one of the most essential but error-prone steps in InSAR processing. The purpose of PU is to calculate the absolute phase values from the original wrapped phase. The success or failure of PU can directly influence the plausibility of the final product (either a topography map or a deformation map).

Theoretically, if the phase gradient is continuous, meaning spatial continuity, in the imaged area, there will be no problem calculating an absolute phase gradient (Itoh, 1982). However, in reality, phase noise and steep terrain slopes are inherent problems that cause phase discontinuity and thus hinder the theoretical assumption.

In order to cope with the phase discontinuity problem, it was suggested that one could guide and assist PU algorithms by applying the quality map. According to Ghiglia and Pritt (1998), there are various methods to evaluate the quality of each pixel of a radar image with values ranging from 0 (worst) to 1 (best). The most common quality map is a coherence image (Wolf, 1985). This method could not only reduce the previously jittery phase values but also could increase the calculation speed.

As a result, we make use of coherence threshold to mask out noisy pixels in an interferogram based on coherence maps. By applying coherence thresholds, we set the pixels of which the coherence is under the pre-set threshold to 0 (Wu, 2021).

In our research, we have tested five different thresholds – 0, 0.1, 0.2, 0.3, and 0.4 – and assessed which the product could achieve a better accuracy and relationship between the two discussing parameters.

3.5 Elevation System Conversion

The topography height generated from the InSAR technique should be referred to an ellipsoid (Ferretti et al., 2007). That means the elevation derived from InSAR is measured in ellipsoidal height. Since the height needs to be compared with the referenced LiDAR DEM, which was built using orthometric heights, the measured ellipsoidal heights should be converted to orthometric heights by equation (8) (Kavzoglu and Saka, 2005).

$$H_{ortho} = H - N \quad (8)$$

where H_{ortho} = the orthometric heights
H = the ellipsoidal heights
N = undulation

To conduct the conversion, an undulation model is necessary. In this research, the undulation model provided by The Ministry of the Interior of Taiwan (National Development Council, 2016) has been used.

3.6 Work Frame

The work frame of this study is shown in Figure 2.

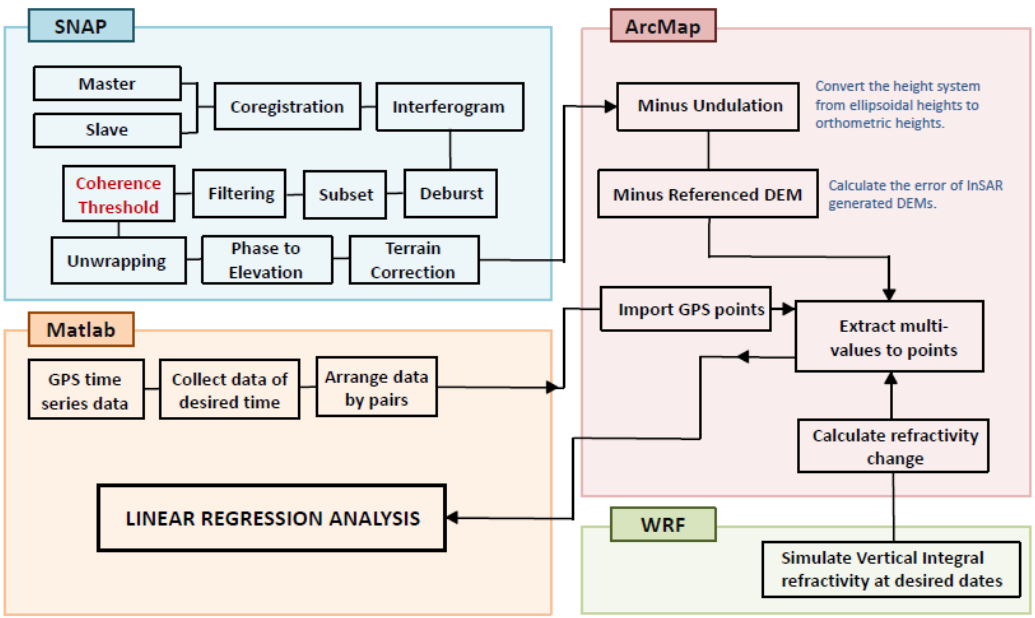

Figure 2. Work frame the study

4. DATA

4.1 Sentinel-1 Images

C-band Sentinel-1A imagery was chosen as the main source of data. Since there are no Sentinel-1B images available that cover the area of interest, only Sentinel-1A images were used. Eight pairs of descending Sentinel-1A images were selected to reach a 12-day temporal baseline. The detailed information is shown in Table 1.

Table 1 Geometric parameters of data

	Pair 1		**Pair 2**	
Master/Slave	Master	Slave	Master	Slave
Date (UTC)	2017.05.29	2017.06.10	2017.06.22	2017.07.04
$B_{\perp}$ (m)	114		114	
	Pair 3		**Pair 4**	
Master/Slave	Master	Slave	Master	Slave
Date (UTC)	2018.12.14	2018.12.26	2019.01.31	2019.02.12
$B_{\perp}$ (m)	139		96	
	Pair 5		**Pair 6**	
Master/Slave	Master	Slave	Master	Slave
Date (UTC)	2019.05.07	2019.05.19	2019.05.31	2019.06.12
$B_{\perp}$ (m)	104		155	
	Pair 7		**Pair 8**	
Master/Slave	Master	Slave	Master	Slave
Date (UTC)	2019.09.28	2019.10.10	2019.10.22	2019.11.03
$B_{\perp}$ (m)	133		113	

4.2 GPS Data

There are 539 GPS stations in total located all over Taiwan, covering the time period from 1993 to 2019 (Figure 2). Because the area of the study site is small, there are only three GPS stations (denoted as red dots in Figure 4) located within the interest area.

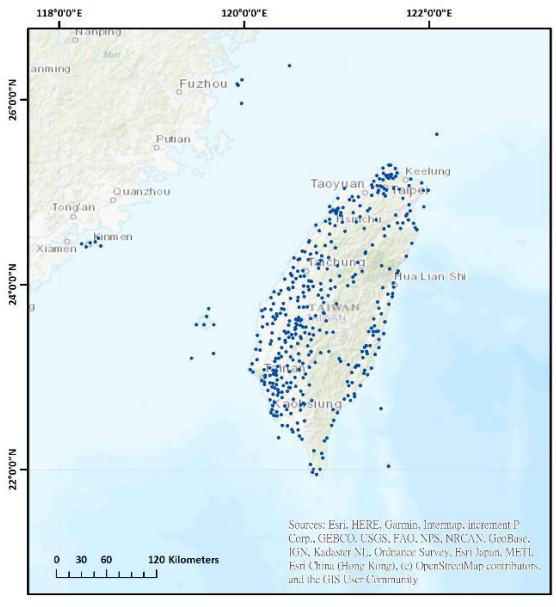

Figure 3. 539 GPS station cover all part of Taiwan. (source: ESRI ArcMap and data sources cited therein)

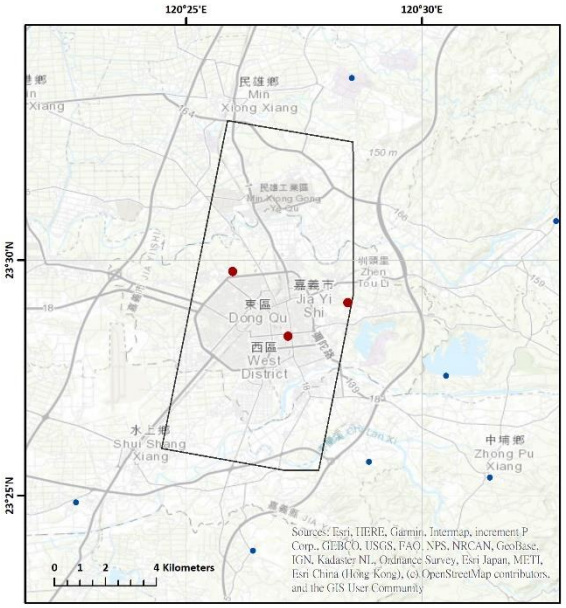

Figure 4. 3 GPS stations located inside of the test site. (source: ESRI ArcMap and data sources cited therein)

4.3 Integral Refractivity

Based on work publish by Liu et al. (2016), the hydrostatic (N_{hydr}) and wet (N_{wet}) tropospheric delay were computed from the WRF model which is developed in-house.

The model utilized Global Forecast System (GFS) data with 0.25 degree to set the initial and boundary condition of the parent WRF domain. In order to reduce the error of the initial field, Grid-point Statistical Interpolation (GSI v3.5) three-dimensional variational data assimilation (3DVAR) system is manipulated to assimilate the observation data collected by two sensors, Cross track Infrared Sounder (CrIS) and Advanced Technology Microwave Sounder (ATMS), which provide the atmospheric temperature and moisture information as profiles.

Suomi National Polar-orbiting Partnership (SNPP), the satellite which carries CrIS and ATMS, passes (descending) through Taiwan every day at around 18:00 UTC. Since the data acquisition time of Sentinel-1 is at about 21:52 UTC, we used the observation data of SNPP collected at 18:00 UTC as the initial field.

The WRF model domain was configured with three one-way nested domains with horizontal resolution of 27, 9 and 3km. Besides, a terrain following vertical coordinate (i.e. eta-level) with 35 layers were adopted, of which the top level is 30 hPa. Owing to the fact that the study site is small, we employed the data of 3 km resolution.

5. RESULTS

5.1 SAR-based Digital Elevation Models

In order to alleviate the influence of the error produced by PU, we have tried to derive InSAR-DEMs with five different coherence thresholds (denoted as THOLD): 0, 0.1, 0.2, 0.3 and 0.4. In each pair, 8000 random points were selected to calculate the RMS error. Figure 5 demonstrates the RMS error of each pair. From Figure 4, we can see that except for pair 4 (190131), all the other pairs have shown that as the coherence threshold is larger,

the measured elevation is more accurate. Overall, the coherence mask can improve the accuracy up to 52.61%.

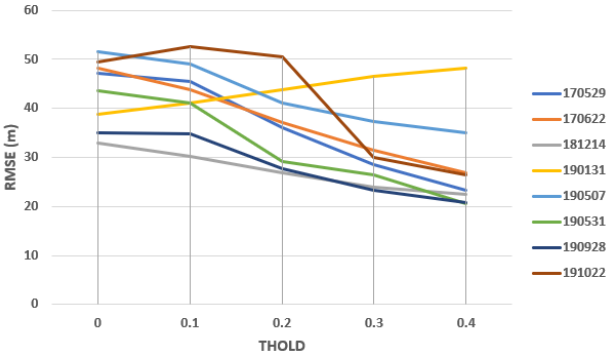

Figure 5. The RMS error of different coherence thresholds.

To illustrate, the error map of pair 5 (190507) is displayed in Figure 6. The gradual color scale ranges from red over white to blue pattern with 100 m as maximum and -100 m as minimum. The pixel is shown in red if the InSAR-DEM is overestimated, while it shows in blue if underestimated. White pixels represent correctly estimated pixels values.

Figure 6 explains why the threshold could help to improve the accuracy. The apparent unwrapping errors appeare as dark red blocks or dark blue blocks when no threshold is applied. They are largely reduced except for a patch of overestimation at the upper right corner when the threshold is 0.4.

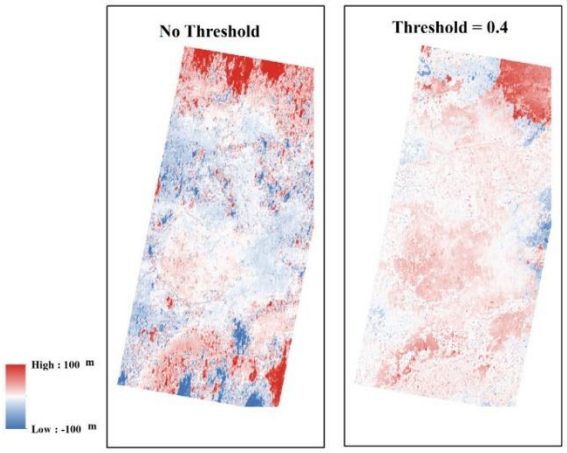

Figure 6. Error map of pair 5 (190507) as an illustration.

When the coherence threshold is set, the pixels that are lower than the threshold are set to zero. This could significantly decrease the occurrence of phase discontinuity, thus the block patters are greatly reduced as the coherence threshold is higher. As for the reason why pair 4 (190131) showed an opposite result, we have a few preliminary assumptions which are also related to the phase discontinuity problems. This issue is one of our further investigation topics.

5.2 Regression Analysis

To conduct regression analysis, the GPS points of the study sites are collected as regression points. Since there are 3 GPS Stations inside of the experimental area, and 8 pairs of InSAR-DEMs are generated, there are 24 points in total for regression analysis.

Figure 7 illustrates the frequency of the height error. From the distribution, we can see that the error is normalized distributed. Only few large errors occur, which we consider as PU error.

Although the coherence thresholds were used to reduce the PU errors, the errors still exist in the interferograms and lead to obvious misrepresentations of terrain heights as shown in Figure 4. In order not to let the points which are contaminated by large PU errors interfere with the regression results, we calculated the standard deviation (SD) of each pair and remove the point whose errors are larger than SD.

As the distribution of height error shown in Figure 5 is quite concentrated, we have tested to remove the points whose absolute values are larger than 1SD, 0.75 SD, or 0.5 SD.

From equation (5), we observe a linear relationship between height error and the influencing factors. Thus, a linear regression model formula is built and equation (9) is formed.

$$Y = aX_1 + bX_2 \quad (9)$$

where Y = height error
X_1 = surface deformation in LOS direction
X_2 = vertical integral refractivity

The outcome of the regression model is demonstrated in Figure 8. As the experiment shows, when the coherence threshold is 0.3 and the points were filtered with 0.5 SD, the R^2 can achieve up to 0.85. Overall, however, $R^2$is not ideal as expected.

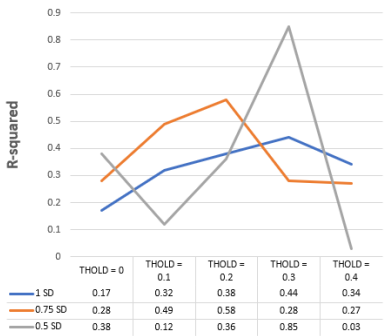

Figure 8. The R^2 value of each coherence threshold

If we only look into the relationship between the height error and either factor (Figure 9, take 0.5 SD as an example) by calculating correlation coefficient (r), we can easily observe that the relationship between error and surface deformation is much more apparent than integral refractivity. There are two reasons for this: (1) three apparent groups of refractivity variation at around -0.15, 0 and 0.1 can be observed. Since the change of refractivity cannot vary dramatically spatially, the points can only be dispersed if more different pairs are chosen; (2) one of the groups of refractivity variation are near zero, contributing limited information for the regression model. In other words, there are fewer points for us to observe the relationship between large refractivity variation and the error.

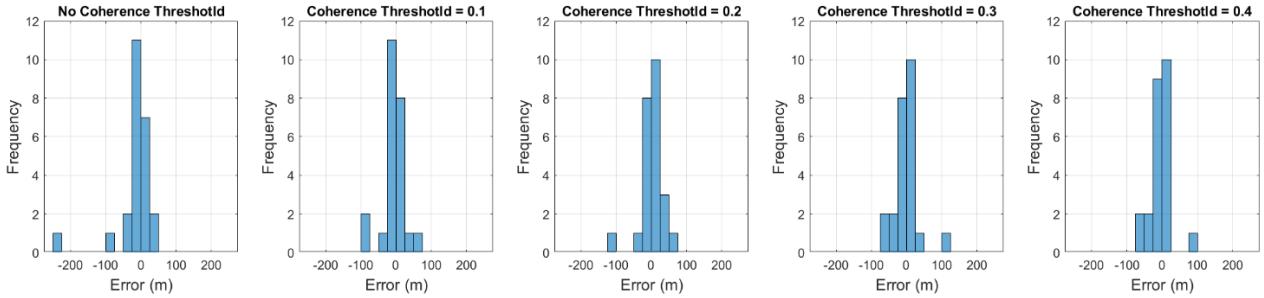

Figure 7. The error frequency distribution.

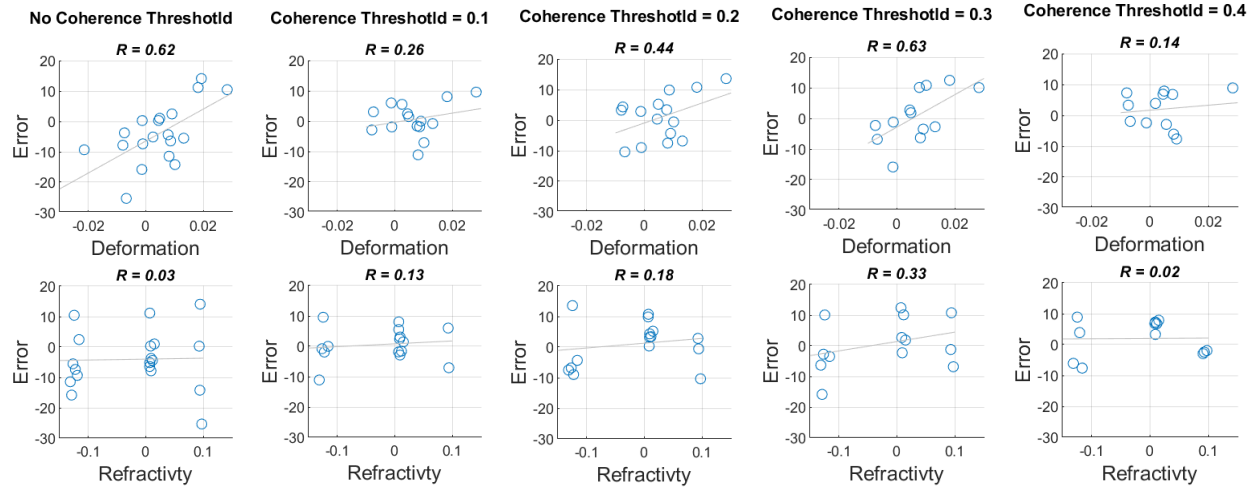

Figure 9. Relationship between height error and either factor (deformation or refractivity). Take the comparison of 0.5 SD as an example.

6. CONCLUSION AND DISCUSSION

In this research, we conducted a linear regression analysis based on a formal description that attempts to explain the relationship between height error of InSAR-DEMs and the controlling factors. We also applied the coherence threshold during InSAR processing to alleviate the impact of phase unwrapping error, which was proved to be effective since the RMS values are significantly reduced as the threshold is raised.

Despite the outcome of the regression analysis, it remains challenging to find a general trend which would have been in accordance with the modelled relationship constructed in equation (5). Besides, the correlation coefficient shows that more apparent relationship between error and deformation can be found, while we can hardly find any relationship between error and integral refractivity.

We conclude that the following reasons might have contributed to this outcome:

First of all, according to Hanssen (2001), after we derive equation (4), we could further obtain the propagation of an error in the interferometric phase to topographic height difference (Equation 10). To incorporate the two controlling factors into equation (10), some careful derivations are needed to be done.

$$\sigma_H^2 = \left(-\frac{\lambda R sin\theta}{4\pi B_\perp}\right)^2 \sigma_\varphi^2 \qquad (10)$$

where σ_H = the variance of topographic height
σ_φ = the phase variance

Secondly, the error caused by phase unwrapping is still a problem although a small urban area was chosen and the coherence thresholds are applied. Instead of removing the points with large errors based on standard deviation, a more reasonable judgement needs to be developed in order not to keep the points of interest.

Thirdly, as there are only three GPS stations within the study area, and eight pairs of Sentinel-1 images were processed, we have limited points to conduct regression analysis. It would likely be more beneficial if more points, which means more various deformation and refractivity data, could be included into the model.

One of the major problems of this research is that there are too many uncontrollable factors and assumptions, thus the experiment is challenging since we might not obtain the result that we hope for. Nevertheless, we still believe that it is an interesting work that worth exploring.

ACKNOWLEDGEMENTS

We thank Professor Chian-Yi Liu Shen-Cha Hsu for developing the WRF model and produce vertical integral refractivity in favour of this research.

REFERENCES

Bekaert, D., Walters, R., Wright, T., Hooper, A., Parker, D., 2015. Statistical comparison of InSAR tropospheric correction techniques. Remote Sensing of Environment 170, 40-47.

Ferretti, A., Monti-Guarnieri, A., Prati, C., Rocca, F., 2007. InSAR Principles: Guidelines for SAR Interferometry Processing and Interpretation, 19 vols. The Netherlands: ESA Publications.

Ghiglia, D.C., Pritt, M.D., 1998. Two-dimensional phase unwrapping: theory, algorithms, and software. Wiley New York.

Chen, H.Y., 2019. GPS LAB. http://gps.earth.sinica.edu.tw (11 December 2020).

Hanssen, R.F., 2001. Radar interferometry: data interpretation and error analysis. Springer Science & Business Media.

Hu, J., Li, Z., Ding, X., Zhu, J., Zhang, L., Sun, Q., 2014. Resolving three-dimensional surface displacements from InSAR measurements: A review. Earth-Science Reviews 133, 1-17.

Itoh, K., 1982. Analysis of the phase unwrapping algorithm. Applied optics 21, 2470-2470.

Kavzoglu, T., Saka, M., 2005. Modelling local GPS/levelling geoid undulations using artificial neural networks. Journal of geodesy 78, 520-527.

Li, F.K., Goldstein, R.M., 1990. Studies of multibaseline spaceborne interferometric synthetic aperture radars. IEEE Transactions on Geoscience and Remote Sensing 28, 88-97.

Liu, C.-Y., Kuo, S.-C., Lim, A.H., Hsu, S.-C., Tseng, K.-H., Yeh, N.-C., Yang, Y.-C., 2016. Optimal use of space-borne advanced infrared and microwave soundings for regional numerical weather prediction. Remote Sensing 8, 816.

Organisation météorologique, m., 1992. International meteorological vocabulary. Secretariat of the World Meteorological Organization, Geneva.

Rodriguez, E., Martin, J., 1992. Theory and design of interferometric synthetic aperture radars, IEE Proceedings F (Radar and Signal Processing). IET, pp. 147-159.

Skamarock, W.C., Klemp, J.B., Dudhia, J., Gill, D.O., Barker, D.M., Wang, W., Powers, J.G., 2008. A description of the Advanced Research WRF version 3. NCAR Technical note-475+ STR.

Smith, E.K., Weintraub, S., 1953. The constants in the equation for atmospheric refractive index at radio frequencies. Proceedings of the IRE 41, 1035-1037.

SNAP development team, 2020. SNAP Software, Version 8.0.0. https://step.esa.int/main/download/snap-download/ (14 April 2021).

Thayer, G.D., 1974. An improved equation for the radio refractive index of air. Radio Science 9, 803-807.

Usai, S., 1997. The use of man-made features for long time scale INSAR, IGARSS'97. 1997 IEEE International Geoscience and Remote Sensing Symposium Proceedings. Remote Sensing-A Scientific Vision for Sustainable Development. IEEE, pp. 1542-1544.

Wolf, J., 1985. Born again group testing: Multiaccess communications. IEEE Transactions on Information Theory 31, 185-191.

Wright, T., Fielding, E., Parsons, B., 2001. Triggered slip: observations of the 17 August 1999 Izmit (Turkey) earthquake using radar interferometry. Geophysical Research Letters 28, 1079-1082.

Wu, Y. Y. (2021). Filter out low coherence pixels before phase unwrapping (STEP Forum). https://forum.step.esa.int/t/filter-out-low-coherence-pixels-before-phase-unwrapping/28759 (3 March 2021)

Zebker, H.A., Goldstein, R.M., 1986. Topographic mapping from interferometric synthetic aperture radar observations. Journal of Geophysical Research: Solid Earth 91, 4993-4999.

Zebker, H.A., Villasenor, J., 1992. Decorrelation in interferometric radar echoes. IEEE Transactions on geoscience and remote sensing 30, 950-959.